Clocking the intrinsic time of multiphoton ionization in linearly polarized fields

Peipei Ge,[1] Yankun Dou,[1] Meng Han,[1] Yiqi Fang,[1] Zhenning Guo,[1] Chengyin Wu,[1,2,3] Qihuang Gong,[1,2,3] and Yunquan Liu[1,2,3,4]

[1]*State Key Laboratory for Mesoscopic Physics and Frontiers Science Center for Nano-Optoelectronics, School of Physics, Peking University, Beijing 100871, China*

[2]*Collaborative Innovation Center of Extreme Optics, Shanxi University, Taiyuan, Shanxi 030006, China*

[3]*Center for Applied Physics and Technology, HEDPS, Peking University, Beijing 100871, China*

[4]*Beijing Academy of Quantum Information Sciences, Beijing 100193, China*

(Received 15 June 2022; revised 10 October 2022; accepted 18 October 2022; published 1 November 2022)

We investigate the subcycle temporal property of multiphoton ionization of Ar atoms in a linearly polarized laser pulse at 400 nm by employing the two-color phase-of-the-phase photoelectron spectroscopy. A perturbative weak 800-nm circularly polarized field is used to clock the intrinsic multiphoton ionization dynamics. The resulting phase-of-the-phase spectrum under this field configuration reveals a prominent angular-dependent feature. We show that the angular-dependent phase-of-the-phase is associated with the phase difference of photoelectron intracycle interference. This enables us to access the complex phase of the photoelectron wave packet of multiphoton ionization. The intrinsic complex ionization time of strong-field approximation has been retrieved for above-threshold ionization.

DOI: 10.1103/PhysRevA.106.053102

I. INTRODUCTION

Strong-field ionization of atoms and molecules is a fundamental process in light-matter interaction. It triggers plenty of ultrafast phenomena in strong-field physics, such as photoelectron holography [1], laser-induced electron diffraction [2,3], and the generation of the attosecond laser pulses [4,5], paving the way for attosecond science. The ionization time as a paramount parameter in the ionization process characterizes the intrinsic temporal property of strong-field ionization. In the classical trajectory model, the strong-field ionization is often assumed to occur instantaneously. And the ionization instant is a real number. Whereas in the quantum-orbit model [6], based on Feynman's path integral, the ionized electron follows a complex trajectory and the ionization time t_s which is derived from the saddle-point equation is complex. The real part of the ionization time t_r corresponds to the instant when the electron is released from atoms. The imaginary part t_i is related to the Keldysh time quantifying the motion of electrons under the potential barrier [7]. It is associated with the ionization probability at the ionization exit. In strong-field approximation (SFA) theory [8], the complex ionization time determines the electron initial momentum and position at the ionization exit, which influence the subsequent dynamic processes and would result in the nonadiabatic effects in strong-field ionization [9–11].

With the advances in attosecond time-resolved methods [12–16], precisely timing the electron release in the strong-field ionization process has become possible. For example, the proposal of attoclock technique has enabled the measurement of ionization instant in strong-field ionization by circularly or elliptically polarized laser pulses [15,17–20]. Specifically, it measures the real time delay for electrons that tunnel at the maximum of the electric field. Besides that, the two-color (ω, 2ω) high-order-harmonic generation (HHG) spectroscopy [21,22] and the photoelectron holograph [23–26] have also been applied to time resolve ultrafast ionization dynamics. In both methods, the two-color phase-dependent HHG or photoelectron signal is analyzed. This kind of working principle is an analogy to that of recently introduced two-color phase-of-the-phase (POP) photoelectron spectroscopy [27], which has been demonstrated as a powerful tool in probing the structure information of atoms and molecules [27–32].

Up to now, most of time-resolved investigations based on aforementioned methods have focused on tunneling ionization. In the multiphoton regime, the electrons can be ionized via simultaneously absorbing multiple photons exceeding the ionization threshold, leading to the well-known above-threshold ionization (ATI) process [33]. In contrast to tunneling ionization, the electron rescattering in multiphoton ionization is largely suppressed. Thus, the time-resolved methods which are based on electron rescattering are not suitable to resolve multiphoton ionization dynamics. Recently, the time delay between adjacent ATI channels has been probed with a reconstruction of attosecond beating by interference of two-photon transition (RABBITT)-like scheme [34]. Characterizing the temporal property of multiphoton ionization especially the ATI process is crucial for understanding the quantum phenomenon in strong-field physics, and it would have implications for real-time imaging the atomic wave function.

In this paper, we employ a perturbative weak 800-nm circular field to clock multiphoton ionization dynamics of Ar atoms induced by the 400-nm linearly polarized field [as described in

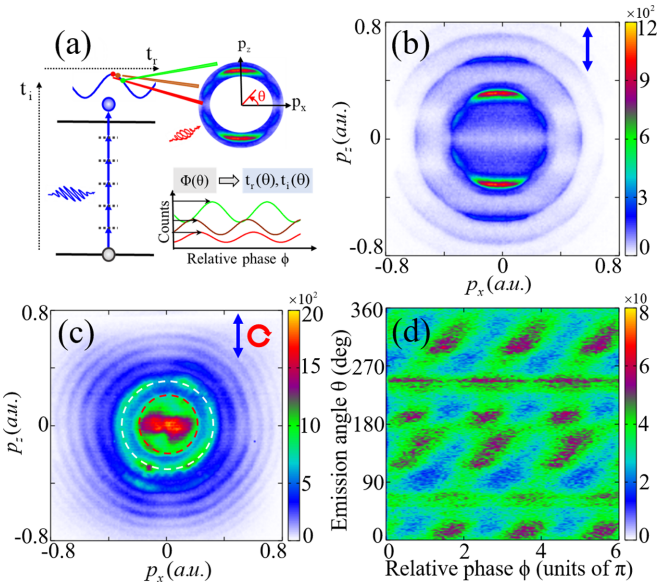

FIG. 1. (a) Scheme for clocking multiphoton ionization dynamics with two-color POP spectroscopy. Here, a strong 400-nm linearly polarized field is employed to trigger the multiphoton ATI process, whereas a weak 800-nm circular field is introduced to perturb the subcycle ionization dynamics. In particular, the rotating 800-nm electric-field vector would map different ionization instant to different electron emission angle θ. By analyzing the two-color phase-dependent photoelectron angular distribution via the POP spectroscopy, the temporal property of multiphoton ionization can be revealed. (b) and (c) Measured photoelectron momentum distributions (PMDs) of multiphoton ionization of Ar atoms in 400-nm linearly polarized fields and in two-color fields. The field polarization configurations are labeled. The white and red dashed lines in (c) denote the positions of the first-order ATI ring and sideband, respectively. (d) Measured two-color phase-resolved photoelectron angular distribution of the first-order ATI ring.

Fig. 1(a)]. The rotating 800-nm electric-field vector angularly streaks the liberated electrons and maps the ionization instants to different emission angles. By varying the relative phase between the two colors, the fundamental field introduces a controllable perturbation that probes the underlying temporal dynamics of the ATI. Specifically, we analyze the two-color phase-dependent PMDs via the POP spectroscopy. The resulting POP under this field configuration exhibits prominent angular and energy dependences. Based on the SFA theory within the saddle-point approach, we show that the angular-dependent POP at the ATI peaks links to the phase difference of intracycle interference. This enables the reconstruction of the complex phase of ATI electrons and, thus, the related complex ionization time. Our approach provides a scheme for time resolving the multiphoton ionization dynamics on the attosecond timescale.

II. EXPERIMENTAL SETUP

Experimentally, the fundamental laser pulses (800 nm, 25 fs, and 3 kHz) are delivered from a Ti:sapphire femtosecond laser system. The second harmonic pulses at 400 nm are generated by frequency doubling through a 250-μm-thick β-barium borate crystal. The two-color laser fields are realized using a Mach-Zehnder interferometry. In each arm, a $\lambda/2$ plate, a wire grid polarizer, and a $\lambda/4$ plate are successively installed in order to separately control the laser intensity and field polarization of the beam. We use a pair of fused silica wedges to finely adjusting the relative phase ϕ between the two-color laser pulses. The two-color synthesized fields can be given by $\boldsymbol{E}(t) = [E_{400}\cos(2\omega t + \phi) + E_{800}\cos(\omega t)]\boldsymbol{z} + E_{800}\sin(\omega t)\boldsymbol{x}$ within plane approximation. Then, the fields are focused onto the supersonic gas jet of Ar atoms by a concave mirror with a focal length of 75 mm. The three-dimensional momentum distributions of the charged ions and photoelectrons are coincidently measured using the cold-target recoil ion momentum spectroscopy [35]. The laser intensity of 400-nm linearly polarized field is calibrated to be 7.11×10^{13} W/cm^2 ($E_{400} = 0.045$ a.u., where (a.u.) stands for atomic units) according to the location of ATI peaks. Whereas the laser intensity of the 800-nm circular pulse is estimated to be 1.8×10^{12} W/cm^2 ($E_{800} = 0.005$ a.u.) by comparing the measured PMDs in two-color fields with the calculated solution of the time-dependent Schrödinger equation. a.u. are used throughout otherwise specified.

III. EXPERIMENTAL RESULTS AND THEORETICAL CALCULATIONS

Figure 1(b) shows the measured PMD of multiphoton ionization of Ar atoms in 400-nm linearly polarized fields. Clearly, the PMD is dominant by a series of ATI rings with distinct angular distribution. The angular-modulated ATI rings can be viewed as the consequence of the interplay between intercycle and intracycle interferences [36]. Whereas the former gives rise to the well-known ATI peaks, the latter leads to the angular modulation on ATI rings providing the information on subcycle ionization dynamics. We then introduce a weak 800-nm right-handed circular field to probe the multiphoton ionization dynamics at 400 nm. The relative phase between the two colors is finely tuned. Figure 1(c) displays the measured phase-integrated PMD in two-color fields. Compared to the result in a single 400-nm field, the sidebands arise between the adjacent 400-nm ATI peaks. Moreover, the interference pattern on PMD is modified. It rotates angularly and becomes asymmetric with respect to the polarization direction (z axis) of 400-nm laser pulses in the two-color synthesized fields. Such rotation can be attributed to the influence of the Coulomb potential during the electron's propagation in the continuum [37].

To clearly visualize the modulation on PMD induced by the weak clocking field, we take the first-order ATI ring as an example and show its angular distribution with respect to the relative phase ϕ between the two-color laser fields in Fig. 1(d). Here, the emission angle is defined as $\theta = \arctan(p_z/p_x)$. For each emission angle θ, the photoelectron yield oscillates with respect to ϕ, following an function of $Y(\theta, \phi) = Y_0(\theta) + \Delta Y(\theta)\cos(\phi + \Phi)$, where $Y_0(\theta)$ is the background count, $\Delta Y(\theta)$ is the relative phase contrast (RPC), and Φ is the so-called phase-of-the-phase. Mathematically, the POP spectroscopy can be realized by fast-Fourier-transforming $Y(\theta, \phi)$ with respect to ϕ for each θ [27]. We utilize this method to analyze the phase-dependent angle-resolved

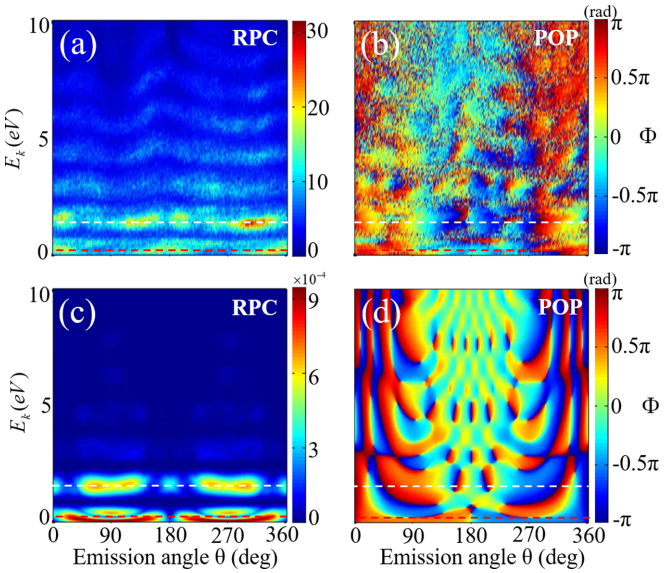

FIG. 2. Experimental angle- and energy-resolved (a) RPC and (b) POP spectra retrieved from the phase-resolved photoelectron spectra. Calculated (c) RPC and (d) POP spectra based on the SFA model. The white and red dashed lines indicate the positions of the first-order 400-nm ATI peak and sideband, respectively.

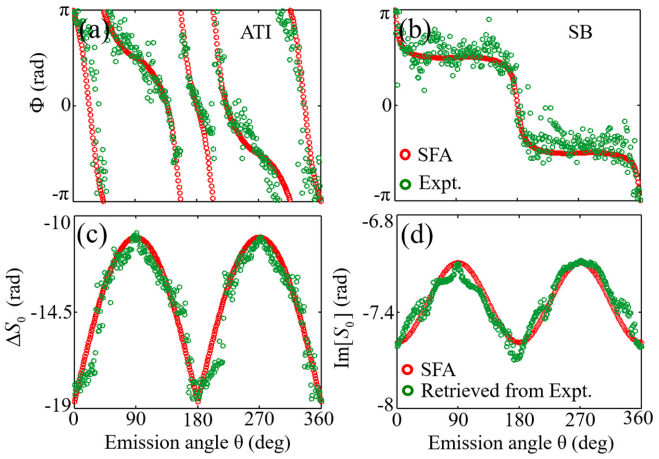

FIG. 3. Angle-resolved POP spectra for (a) the first-order ATI ring and (b) the sideband. Angle-resolved (c) phase difference ΔS_0 and (d) imaginary phase Im[S_0] for the first-order ATI ring. The red and green circles denote the SFA-calculated results and experimental results, respectively.

photoelectron energy spectra. The resulting RPC and POP spectra are shown in Figs. 2(a) and 2(b), respectively. The overall structure of RPC resembles the interference pattern of the phase-integrated PMD as shown in Fig. 1(c). As for the POP spectrum, prominent angle-, and energy-dependent features are revealed, which are different from the reported POP spectra in previous investigations [27–32].

To understand the experimental POP spectrum, we resort to the SFA theory which has been verified to work well in the multiphoton regime [28,34]. Details of the calculation using SFA theory are included in Appendix A. Figures 2(c) and 2(d) illustrate the retrieved RPC and POP spectra from the phase-resolved SFA calculations. One can observe the calculated RPC spectrum basically reproduces the main structure of the experimental RPC spectrum. Similar to the experimental POP spectrum, the calculated POP spectrum also exhibits prominent angular and energy dependences. Since the Coulomb effect has been ignored in the SFA, the angular shifts of the experimental RPC and POP spectra at lower electron energies have not been captured by the calculations.

For quantitative comparison between the SFA calculation and the experiment, we select the first-order ATI ring and sideband and show their angle-resolved POP spectra in Figs. 3(a) and 3(b), respectively. Note that the experimental spectra have been angularly rotated with a certain angle in order to deduct the influence of the Coulomb potential. The rotated angle depends on the photoelectron energy and can be obtained by comparing the experimental RPC spectrum with the calculated as shown Figs. 2(a) and 2(c). For the first-order ATI ring as depicted in Fig. 3(a), the value of POP experiences rapid variations with respect to the emission angle. Whereas for the sideband as shown in Fig. 3(b), Φ almost remains unchanged within the regions of [0°,180°] and [180°,360°], and the value in these two regions differs by π. Such angular dependences of the experimental POP spectra are well captured by the SFA calculation (red circles). Within the saddle-point approach, these angular- and energy-dependent features can be understood in terms of the quantum orbits [6]. In the following, we focus on the angular-dependent POP spectrum of 400-nm ATI rings in order to shed light on ionization dynamics of the ATI process.

IV. DISSCUSSION

In single 400-nm linearly polarized fields, the angular modulation on ATI rings results from the intracycle interference between two quantum orbits released within the same cycle with their ionization instants labeled as t_{s1} and t_{s2}. After adding a weak 800-nm circular field, the phase of each orbit is perturbed with $S(\boldsymbol{p}, t_s, \phi) = S_0(\boldsymbol{p}, t_s) + \delta(\boldsymbol{p}, t_s, \phi)$, where $S_0(\boldsymbol{p}, t_s)$ denotes the complex phase in single 400-nm fields, and $\delta(\boldsymbol{p}, t_s, \phi)$ is the additional action induced by the weak 800-nm field. Given that the weak 800-nm circular field has little influence on the ionization amplitude, the intracycle interference can be expressed as $I(\boldsymbol{p}, \varphi) = |e^{iS_1} + e^{iS_2}|^2 = 2W_0^2 + 2W_0^2 \cos(\mathrm{Re}[S_1] - \mathrm{Re}[S_2])$ with $W_0 = e^{-\mathrm{Im}[S_{01}]} = e^{-\mathrm{Im}[S_{02}]}$ representing the ionization amplitude of quantum orbit in single 400-nm fields. In this expression, only the phase difference term $\mathrm{Re}[S_1] - \mathrm{Re}[S_2]$ is two-color phase dependent and we can further expand it into

$$\begin{aligned}\mathrm{Re}[S_1] - \mathrm{Re}[S_2] &= \mathrm{Re}[S_{01}] - \mathrm{Re}[S_{02}] + \mathrm{Re}[\delta_1] - \mathrm{Re}[\delta_2] \\ &= \Delta S_0 + a\ \cos\left(\frac{\phi}{2} + c + \theta\right) \\ &\quad + b\ \cos\left(\frac{\phi}{2} - c\right). \end{aligned} \tag{1}$$

Here, $\Delta S_0 = \mathrm{Re}[S_{01}] - \mathrm{Re}[S_{02}]$ represents the phase difference between the unperturbed intracycle-interfering orbits in single 400-nm linearly polarized fields, $a = \frac{2E_{800}}{\omega^2} p_r \sin\frac{\omega\,\Delta\tau_r}{2} \cosh(\omega t_{i1})$ with $\Delta\tau_r = t_{r2} - t_{r1}$ and

$p_r = \sqrt{p_x^2 + p_z^2}$ as the radial momentum, $c = \omega(t_{r2} + t_{r1})$ is a constant which equals $\pi/4$ for the $p_z > 0$ plane and $3\pi/4$ for the $p_z < 0$ plane and $b = \frac{E_{400}E_{800}}{2\omega^3}[\sin(\frac{\omega\,\Delta\tau_r}{2})\cosh(\omega t_{i1}) + \frac{1}{3}\sin(\frac{3\omega\,\Delta\tau_r}{2})\cosh(3\omega t_{i1})]$. For each momentum $\boldsymbol{p}$, the term ΔS_0 and the coefficients a and b are constants. The POP spectroscopy monitors the two-color phase when the photoelectron signal reaches maximum, and, thus, this requires $\mathrm{Re}[S_1] - \mathrm{Re}[S_2] = 2m\pi$ (m is an integer). To satisfy this condition, the two-color phase ϕ needs to match the value of ΔS_0 with $a\cos(\frac{\phi}{2} + c + \theta) + b\cos(\frac{\phi}{2} - c) = 2m\pi - \Delta S_0$. This indicates the angular-dependent POP actually reflects the information of ΔS_0. Within the SFA model, ΔS_0 can also be analytically derived as

$$\begin{aligned}\Delta S_0 = &-(E_k + U_p + I_p)\Delta\tau_r \\ &- \frac{2p_r E_{400}}{\omega_{400}^2}\cos(2\omega t_{r1})\cosh(2\omega t_{i1})\sin\theta \\ &+ \frac{E_{400}^2}{4\omega_{400}^3}\sin(4\omega t_{r1})\cosh(4\omega t_{i1}),\end{aligned} \tag{2}$$

with $U_p = E_{400}^2/4/\omega^2$ as the pondermotive energy induced by the 400-nm linearly polarized fields and I_p as the ionization potential. From this expression, one can see ΔS_0 contains very important information of the multiphoton ATI, which is associated with the complex ionization time t_{s1}. Thus, retrieving ΔS_0 from the angular-dependent POP is the central to revealing the complex ionization time of ATI electrons.

We now concentrate on the first-order ATI ring and utilize its angular-dependent POP spectrum to retrieve the phase difference ΔS_0. Before retrieval, we present the calculated ΔS_0 (red circles) in Fig. 3(c). One can observe ΔS_0 shows a clear angular dependence. It reaches maximum (minimum) when the emission direction is parallel (perpendicular) to the polarization axis of the 400-nm field. Then, we establish the quantitative relationship between ΔS_0 and angular-dependent POP within the SFA theory (as presented in Appendix B), i.e., $|\Phi| = \{\arccos[\cos(\Delta S_0)]\}$ for the emission angles located within [90°, 270°] or $\{\arccos[\cos(\Delta S_0)]\} = \pi - |\Phi|$ for the rest emission angles. Based on this relationship, one can easily obtain the value of $\{\arccos[\cos(\Delta S_0)]\}$ from the measured POP spectrum. Whereas to access the real value of ΔS_0, one needs to turn back to Eq. (2). The retrieval begins from the emission angle $\theta = 0°$ or 180°. At these emission angles, $p_z = 0$ and the corresponding ionization instants are located at the extrema of the electric field. Consequently, $\Delta\tau_r = T_{400}/2$ and $\Delta S_0 = -(E_k + U_p + I_p)\Delta\tau_r = -n\pi$ (n is the number of absorbed photons during the ATI process). For the first-order ATI ring, $n = 6$. Thus, $\Delta S_0(\theta = 0°,\ 180°) = -6\pi$. From the two emission angles, one can retrieve the angular-resolved ΔS_0 from $\{\arccos[\cos(\Delta S_0)]\}$ by referring to the angular dependence of calculated ΔS_0. As shown in Fig. 3(c), the retrieved ΔS_0 (green circles) shows good agreement with the calculated. It indicates the validity of retrieving ΔS_0 from the angular-dependent POP spectrum.

In 400-nm linearly polarized fields, the interference among the quantum orbits emitting from N cycles at the ATI peaks can be written as $I(\boldsymbol{p}) = |\sum_{k=1}^{2N} e^{iS_k}|^2 = 2N^2W_0^2[1 + \cos(\Delta S_0)]$ [see Appendix C]. Experimentally, the ionization probability $I(\boldsymbol{p})$ at each final momentum $\boldsymbol{p}$ can be obtained

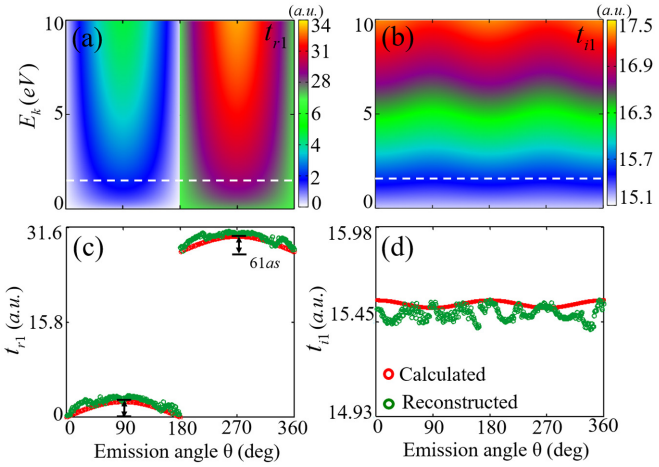

FIG. 4. Angle- and energy-resolved (a) real part t_{r1} and (b) imaginary part t_{i1} of the complex ionization time t_{s1}. The color scale indicates the ionization time (atomic units). The extracted angle-resolved (c) t_{r1} and (d) t_{i1} for the first-order ATI electrons. The red and green circles respectively represent the calculated and reconstructed ionization times.

through dividing the measured electron counts by the total electron counts collected in PMD as shown in Fig. 1(b). The employed 400-nm linearly polarized laser field in our experiment has about 20-cycle pulse duration, i.e., $N = 20$. Then, using the retrieved ΔS_0 one can extract the ionization amplitude W_0 of the ATI rings from the measured PMD. Since the ionization amplitude is governed by $W_0 = e^{-\mathrm{Im}[S_0]}$, the imaginary part of the complex phase $\mathrm{Im}[S_0]$ can be further retrieved, which refers to the phase accumulated during the electron's underbarrier motion. Within the SFA theory, $\mathrm{Im}[S_0]$ can be analytically given by

$$\begin{aligned}\mathrm{Im}[S_0] = &-2(E_k + U_P + I_p)t_{i1} \\ &+ \frac{p_r E_{400}}{\omega_{400}^2}\sin(\omega_{400}t_{r1})\sinh(\omega_{400}t_{i1})\sin\theta \\ &+ \frac{E_{400}^2}{8\omega_{400}^3}\cos(2\omega_{400}t_{r1})\sinh(2\omega_{400}t_i).\end{aligned} \tag{3}$$

In Fig. 3(d), we show the retrieved $\mathrm{Im}[S_0]$ (green circles) from experiment and the calculated $\mathrm{Im}[S_0]$ (red circles) for the first-order ATI ring, which has good agreement. $\mathrm{Im}[S_0]$ shows a cos-like variation as a function of emission angle.

And, thus, we have seen that the angular-dependent POP spectrum contains the subcycle temporal property of multiphoton ionization. Within the saddle-point approach of the SFA, the complex ionization time of multiphoton ionization can be numerically derived. In Figs. 4(a) and 4(b), we show the calculated angle- and energy-resolved t_{r1} and t_{i1} at the experimental condition, respectively. The intrinsic ionization time of multiphoton ionization exhibits prominent angular and energy dependences.

As to experimentally obtain the complex ionization time as seen in Eqs. (2) and (3), one can numerically reconstruct it from the experimental ΔS_0 and $\mathrm{Im}[S_0]$. In Figs. 4(c) and 4(d), we show the reconstructed t_{r1} and t_{i1} (green circles) for the first-order ATI ring, respectively. For comparison, the

calculated results (red circles) are also presented. The reconstructed t_{s1} agrees well with the calculation. Small discrepancies between them originate from the errors in the retrieval of ΔS_0 and Im$[S_0]$. As illustrated in Fig. 4(c), the ionization instant t_{r1} of the first-order ATI electrons is confined within a small region, i.e., 0∼2.58 a.u. for the $p_z > 0$ plane and 27.58∼30.16 a.u. for the $p_z < 0$ plane, corresponding to a photoemission window with the width of 2.58 a.u. (∼61 as). This reveals the angular-dependent intrinsic delays within an ATI channel. As for t_{i1}, a very slight angular dependence is observed. From that, we show that for the first-order ATI electrons, an imaginary time of 15.5 a.u., corresponding to 373 as, is revealed, quantifying the electrons' underbarrier motion. In our experiment, the Keldysh parameter γ is about 2.7, indicating that it is located in the multiphoton ionization regime. Thus, the retrieved t_{i1} here is not directly interpreted as the Keldysh time since the latter is only valid in tunneling limit. Importantly, we find the retrieved imaginary time and the Keldysh parameter satisfy the relationship of $\gamma = \sinh(\omega t_i)$ which is well suited for nonadiabatic ionization depicted by the Perelomov-Popov-Terent'ev theory [38]. This implies the nonadiabaticity of multiphoton ionization inherent in the SFA theory [39].

V. CONCLUSION

In conclusion, we have clocked the complex ionization dynamics of multiphoton ionization in linear laser field using a weak circular field with POP spectroscopy. By analyzing the two-color phase dependence of the photoelectron signal, we extract the energy-resolved POP spectrum which exhibits a prominent angular-dependent feature. The angular-dependent POP spectrum of ATI rings is related with the phase difference of intracycle interference. This enables us to access the complex phase of ATI electrons in multiphoton ionization with linearly polarized fields from which the complex ionization time has been reconstructed. The paper sheds light on the intrinsic temporal properties of the multiphoton ATI process. This field geometry could be potentially used for clocking the elliptical HHG process and probing the negative travel time of quantum orbits [40].

ACKNOWLEDGMENTS

This work was supported by the NSFC (Grants No. 92050201 and No. 8200906472) and China Postdoctoral Science Foundation (Grant No. 8206300495).

APPENDIX A: THE SFA MODEL AND THE CORRESPONDING CALCULATIONS

In the SFA model, the transition amplitude of photoelectron from the initial ground state $|\psi_0\rangle$ to the final Volkov state $|\psi_{\boldsymbol{p}}^V\rangle$ with a final momentum $\boldsymbol{p}$ can be expressed as the coherent supposition of all quantum orbits when adopting the saddle-point approach, i.e., $M_p \sim \sum_s \rho_s(\boldsymbol{p}) e^{iS(p,t_s)}$. Here, $\rho_s(\boldsymbol{p}) \sim \langle \boldsymbol{p} + \boldsymbol{A}(t_s)|\boldsymbol{r}\cdot\boldsymbol{E}(t_s)|\psi_0(\boldsymbol{r})\rangle$ is the preexponential factor with $\boldsymbol{A}(t_s)$ as the vector potential of the laser field and $\boldsymbol{r}\cdot\boldsymbol{E}(t_s)$ as the laser-field-electron interaction. The saddle-point $t_s = t_r + it_i$ which is governed by the equation $[\boldsymbol{p} + \boldsymbol{A}(t_s)]^2/2 + I_p = 0$ represents the complex ionization instant of the quantum orbit. $S(\boldsymbol{p}, t_s) = -\int_{t_s}^{\infty} [\boldsymbol{p} + \boldsymbol{A}(t)]^2/2 + I_p dt$ is the classical action (or complex phase), and I_p is the ionization potential. Considering the periodicity of the two-color synthesized fields, the quantum orbits emitting within two 800-nm cycles can well reproduce the PMD in two-color fields. In the calculation, the laser intensities of the two colors remain the same as that in experiment, i.e., $E_{400} = 0.045$ a.u., $E_{800} = 0.005$ a.u., and $I_p = 0.579$ a.u. For simplicity, the preexponential factor is omitted when calculating the transition amplitude. The 20 relative phases are sampled within $[0,\ 2\pi]$ in order to obtain the two-color phase-resolved angle-resolved photoelectron energy spectra. Figure 5 shows the calculated angle-resolved photoelectron energy spectra at different

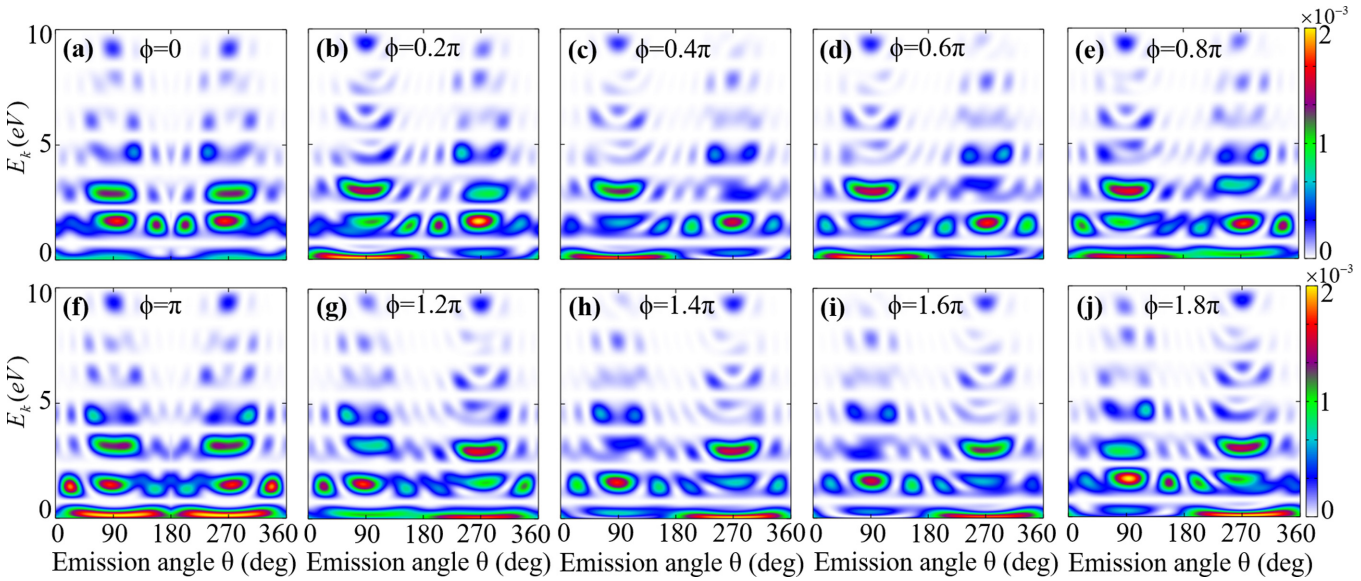

FIG. 5. Calculated angle-resolved photoelectron energy spectra in two-color fields at different relative phases by the SFA model. The relative phase ϕ is labeled.

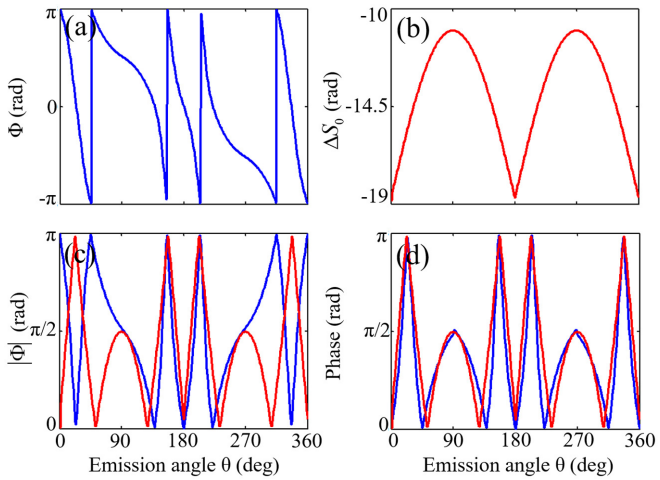

FIG. 6. (a) The angular-resolved POP spectrum for the first-order 400-nm ATI ring retrieved from the SFA calculation. (b) The calculated angular-resolved phase difference ΔS_0 of intracycle interference at the first-order ATI ring. (c) The transformed POP and ΔS_0 which are plotted in the formula of $|\Phi|$ and $\{\arccos[\cos(\Delta S_0)]\}$ with the blue and red lines, respectively. (d) The same as (c) except that the transformed POP within $[0^\circ, 90^\circ]$ and $[270^\circ, 360^\circ]$ takes the formula of $\pi - |\Phi|$.

relative phases. By performing Fourier transformation on these spectra with respect to the relative phase, we obtain the angle- and energy-resolved RPC and POP spectra as shown in Figs. 2(c) and 2(d) in the main text.

APPENDIX B: THE RELATIONSHIP BETWEEN ΔS_0 AND ANGULAR-DEPENDENT POP

We establish the relationship between the phase difference ΔS_0 and the angular-dependent POP within the SFA theory. Figures 6(a) and 6(b) show the calculated Φ and ΔS_0 for the first-order ATI ring, respectively. In order to connect the retrieved POP to ΔS_0, we transform their values into the region of $[0, \pi]$. For the POP, we take its absolute value $|\Phi|$. As for ΔS_0, we convert it by the formula of $\{\arccos[\cos(\Delta S_0)]\}$. The transformed results are depicted in Fig. 6(c). Surprisingly, one can find $|\Phi|$ is almost consistent with $\{\arccos[\cos(\Delta S_0)]\}$ when the emission angle is located within $[90^\circ, 270^\circ]$. Whereas for the rest emission angles ($[0^\circ, 90^\circ]$ and $[270^\circ, 360^\circ]$), the values of the transformed POP and ΔS_0 seem to satisfy the relationship, i.e., $|\Phi| + \{\arccos[\cos(\Delta S_0)]\} = \pi$. In Fig. 6(d), we replot the transformed POP for emission angles located in $[0^\circ, 90^\circ]$ and $[270^\circ, 360^\circ]$ with the formula of $\pi - |\Phi|$. Obviously, the transformed POP well reproduces the value of $\{\arccos[\cos(\Delta S_0)]\}$, demonstrating a direct link between the retrieved POP and ΔS_0.

APPENDIX C: The ANALYTICAL DERIVATION OF THE INTERFERENCE PATTERN IN 400-nm LINEARLY POLARIZED FIELDS

In single 400-nm linearly polarized fields for each momentum $\boldsymbol{p}$, the interference between the two quantum orbits emitting within the same cycle (with the ionization instants labeled as t_{s1} and t_{s2}) corresponds to the intracycle interference, which can be expressed as $I(\boldsymbol{p}) = |e^{iS_1} + e^{iS_2}|^2 = 2W_0^2[1 + \cos(\mathrm{Re}[S_1] - \mathrm{Re}[S_2])]$ with S denoting the complex phase of quantum orbit and $W_0 = e^{-\mathrm{Im}[S_1]} = e^{-\mathrm{Im}[S_2]}$ is the ionization amplitude. Likewise, in the next 400-nm cycle, a pair of quantum orbits arise with the ionization instants satisfying $t_{s3} = t_{s1} + T_{400}$ and $t_{s4} = t_{s2} + T_{400}$. By this analogy, the interference among the quantum orbits emitted from a N-cycle 400-nm laser pulse can be written as $I(\boldsymbol{p}, \varphi) = |\sum_{k=1}^{2N} e^{iS_k}|^2 = |e^{iS_1} + e^{iS_2}|^2 |1 + e^{iS_p} + e^{i2S_p} \cdots + e^{i(N-1)S_p}|^2$ with $S_p = -\int_{t_s}^{t_s+T_{400}} [p + A_{400}(t)]^2/2 + I_p dt = -(E_k + U_p + I_p)T_{400}$ representing the phase difference between the quantum orbits whose ionization instants are separated by T_{400}. For the ATI peaks, $E_k = n\omega_{400} - U_p - I_p$ (n is the number of absorbed photons). Then, $S_p = -2n\pi$ and the interference pattern within the N-cycle laser pulse can be reduced to $I(\boldsymbol{p}, \varphi) = |\sum_{k=1}^{2N} e^{iS_k}|^2 = N^2|e^{iS_1} + e^{iS_2}|^2 = 2N^2W_0^2\{1 + \cos(\mathrm{Re}[S_1] - \mathrm{Re}[S_2])\}$.

[1] Y. Huismans *et al.*, Science **331**, 61 (2011).

[2] C. I. Blaga, J. Xu, A. D. DiChiara, E. Sistrunk, K. Zhang, P. Agostini, T. A. Miller, L. F. DiMauro, and C. D. Lin, Nature (London) **483**, 194 (2012).

[3] B. Wolter, M. G. Pullen, A-T. Le, M. Baudisch, K. D. Dier, A. Senftleben, M. Hemmer, C. D. Schröter, J. Ullrich, T. Pfeifer, R. Moshammer, S. Gräfe, O. Vendrell, C. D. Lin, and J. Biegert, Science **354**, 308 (2016).

[4] M. Hentschel, R. Kienberger, Ch. Spielmann, G. A. Reider, N. Milosevic, T. Brabec, P. Corkum, U. Heinzmann, M. Drescher, and F. Krausz, Nature (London) **414**, 509 (2001).

[5] P. M. Paul, E. S. Toma, P. Breger, G. Mullot, F. Augé, Ph. Balcou, H. G. Muller, and P. Agostini, Science **292**, 1689 (2001).

[6] P. Salières, B. Carré, L. L. Déroff, F. Grasbon, G. G. Paulus, H. Walther, R. Kopold, W. Becker, D. B. Milošević, A. Sanpera, and M. Lewenstein, Science **292**, 902 (2001).

[7] L. V. Keldysh, Sov. Phys. JETP **20**, 1307 (1965).

[8] D. B. Milošević, G. G. Paulus, D. Bauer, and W. Becker, J. Phys. B: At., Mol. Opt. Phys. **39**, R203 (2006).

[9] G. L. Yudin and M. Y. Ivanov, Phys. Rev. A **64**, 013409 (2001).

[10] I. Barth and O. Smirnova, Phys. Rev. A **84**, 063415 (2011); **87**, 013433 (2013).

[11] M. Li, J.-W. Geng, M. Han, M.-M. Liu, L.-Y. Peng, Q. Gong, and Y. Liu, Phys. Rev. A **93**, 013402 (2016); M. Li, M.-M. Liu, J.-W. Geng, M. Han, X. Sun, Y. Shao, Y.i. Deng, C. Wu, L.-Y. Peng, Q. Gong, and Y. Liu, *ibid.* **95**, 053425 (2017).

[12] J. Itatani, F. Quéré, G. L. Yudin, M. Yu. Ivanov, F. Krausz, and P. B. Corkum, Phys. Rev. Lett. **88**, 173903 (2002).

[13] H. G. Muller, Appl. Phys. B: Photophys. Laser Chem. **74**, S17 (2002).

[14] R. Kienberger, E. Goulielmakis, M. Uiberacker, A. Baltuska, V. Yakovlev, F. Bammer, A. Scrinzi, Th. Westerwalbesloh, U.

Kleineberg, U. Heinzmann, M. Drescher, and F. Krausz, Nature (London) **427**, 817 (2004).
[15] P. Eckle, M. Smolarski, P. Schlup, J. Biegert, A. Staudte, M. Schöffler, H. G. Muller, R. Dörner, and U. Keller, Nat. Phys. **4**, 565 (2008).
[16] E. Goulielmakis, Z. H. Loh, A. Wirth, R. Santra, N. Rohringer, V. S. Yakovlev, S. Zherebtsov, T. Pfeifer, A. M. Azzeer, M. F. Kling, S. R. Leone, and F. Krausz, Nature (London) **466**, 739 (2010).
[17] P. Eckle, A. N. Pfeiffer, C. Cirelli, A. Staudte, R. Dörner, H. G. Muller, M. Büttiker, and U. Keller, Science **322**, 1525 (2008).
[18] L. Torlina, F. Morales, J. Kaushal, I. Ivanov, A. Kheifets, A. Zielinski, Armin Scrinzi, H. G. Muller, S. Sukiasyan, M. Ivanov, and O. Smirnova, Nat. Phys. **11**, 503 (2015).
[19] A. N. Pfeiffer, C. Cirelli, M. Smolarski, R. Dörner, and U. Keller, Nat. Phys. **7**, 428 (2011).
[20] U. S. Sainadh, H. Xu, X. Wang, A. Atia-Tul-Noor, W. C. Wallace, N. Douguet, A. Bray, I. Ivanov, K. Bartschat, A. Kheifets, R. T. Sang, and I. V. Litvinyuk, Nature (London) **568**, 75 (2019).
[21] D. Shafir, H. Soifer, B. D. Bruner, M. Dagan, Y. Mairesse, S. Patchkovskii, M. Yu. Ivanov, O. Smirnova, and N. Dudovich, Nature (London) **485**, 343 (2012).
[22] O. Pedatzur, G. Orenstein, V. Serbinenko, H. Soifer, B. D. Bruner, A. J. Uzan, D. S. Brambila, A. G. Harvey, L. Torlina, F. Morales, O. Smirnova, and N. Dudovich, Nat. Phys. **11**, 815 (2015).
[23] G. Porat, G. Alon, S. Rozen, O. Pedatzur, M. Krüger, D. Azoury, A. Natan, G. Orenstein, B. D. Bruner, M. J. J. Vrakking, and N. Dudovich, Nat. Commun. **9**, 2805 (2018).
[24] M. Han, P. Ge, Y. Shao, M.-M. Liu, Y. Deng, C. Wu, Q. Gong, and Y. Liu, Phys. Rev. Lett. **119**, 073201 (2017).
[25] Z. Guo, P. Ge, Y. Fang, Y. Dou, X. Yu, J. Wang, M. Han Q. Gong, and Y. Liu, Phys. Rev. A **104**, L051101 (2021).
[26] Z. Guo, P. Ge, Y. Fang, Y. Dou, X. Yu, J. Wang, Q. Gong, and Y. Liu, Ultrafast Sci. **2022**, 9802917 (2022).
[27] S. Skruszewicz, J. Tiggesbäumker, K.-H. Meiwes-Broer, M. Arbeiter, T. Fennel, and D. Bauer, Phys. Rev. Lett. **115**, 043001 (2015).
[28] M. A. Almajid, M. Zabel, S. Skruszewicz, J. Tiggesbäumker, and D. Bauer, J. Phys. B: At., Mol. Opt. Phys. **50**, 194001 (2017).
[29] V. A. Tulsky, M. A. Almajid, and D. Bauer, Phys. Rev. A **98**, 053433 (2018).
[30] D. Würzler, S. Skruszewicz, A. M. Sayler, D. Zille, M. Möller, P. Wustelt, Y. Zhang, J. Tiggesbäumker, and G. G. Paulus, Phys. Rev. A **101**, 033416 (2020).
[31] V. A.Tulsky, B. Krebs, J. Tiggesbäumker, and D. Bauer, J. Phys. B: At., Mol. Opt. Phys. **53**, 074001 (2020).
[32] M. Han, P. Ge, J. Wang, Z. Guo, Y. Fang, X. Ma, X. Yu, Y. Deng, H. J. Wörner, Q. Gong, and Y. Liu, Nat. Photonics **15**, 765 (2021).
[33] P. Agostini, F. Fabre, G. Mainfray, G. Petite, and N. K. Rahman, Phys. Rev. Lett. **42**, 1127 (1979).
[34] L. J. Zipp, A. Natan, and P. H. Bucksbaum, Optica **1**, 361 (2014).
[35] J. Ullrich, R. Moshammer, A. Dorn, R. Dorner, L. P. H. Schmidt, and H. Schmidt-Bocking, Rep. Prog. Phys. **66**, 1463 (2003).
[36] D. G. Arbó, K. L. Ishikawa, K. Schiessl, E. Persson, and J. Burgdörfer, Phys. Rev. A **81**, 021403(R) (2010).
[37] M. Li, Y. Liu, H. Liu, Q. Ning, L. Fu, J. Liu, Y. Deng, C. Wu, Liang-You Peng, and Q. Gong, Phys. Rev. Lett. **111**, 023006 (2013).
[38] A. M. Perelomov and V. S. Popov, J. Exp. Theor. Phys. **52**, 514 (1967).
[39] M. Y. Ivanov, M. Spanner, and O. Smirnova, J. Mod. Opt. **52**, 165 (2005).
[40] D. B. Milošević and W. Becker, Phys. Rev. A **105**, L031103 (2022).